Geophysical Prospecting

EAGE EUROPEAN ASSOCIATION OF GEOSCIENTISTS & ENGINEERS

Geophysical Prospecting doi: 10.1111/j.1365-2478.2011.01026.x

High-accuracy practical spline-based 3D and 2D integral transformations in potential-field geophysics

Bingzhu Wang[1,2*], Stephen S. Gao[1], Kelly H. Liu[1] and Edward S. Krebes[3]

[1]*Department of Geological Sciences and Engineering, Missouri University of Science and Technology, Rolla, MO 65409, USA,* [2]*GEOTOP-UQAM, Montreal, QC H3C 3P8, Canada, and* [3]*Department of Geoscience, University of Calgary, Calgary, Alberta T2N 1N4, Canada*

Received October 2010, revision accepted September 2011

ABSTRACT

Potential, potential field and potential-field gradient data are supplemental to each other for resolving sources of interest in both exploration and solid Earth studies. We propose flexible high-accuracy practical techniques to perform 3D and 2D integral transformations from potential field components to potential and from potential-field gradient components to potential field components in the space domain using cubic B-splines. The spline techniques are applicable to either uniform or non-uniform rectangular grids for the 3D case, and applicable to either regular or irregular grids for the 2D case. The spline-based indefinite integrations can be computed at any point in the computational domain. In our synthetic 3D gravity and magnetic transformation examples, we show that the spline techniques are substantially more accurate than the Fourier transform techniques, and demonstrate that harmonicity is confirmed substantially better for the spline method than the Fourier transform method and that spline-based integration and differentiation are invertible. The cost of the increase in accuracy is an increase in computing time. Our real data examples of 3D transformations show that the spline-based results agree substantially better or better with the observed data than do the Fourier-based results. The spline techniques would therefore be very useful for data quality control through comparisons of the computed and observed components. If certain desired components of the potential field or gradient data are not measured, they can be obtained using the spline-based transformations as alternatives to the Fourier transform techniques.

Key words: Integral transformations, Cubic B-splines, Gravity, Magnetic, Gravity gradients

INTRODUCTION

The vertical components of the gravity acceleration field and the total-field magnetic data are traditionally measured and the potential-field gradients are increasingly observed for a wide scope of studies in exploration (Nabighian *et al.* 2005a, b). Horizontal derivatives are used for detecting edges of source bodies (Blakely and Simpson 1986; Grauch and Cordell 1987). Both horizontal and vertical derivatives are needed for determining the lateral location and depth of single or multiple simple sources with Euler deconvolution (Thompson 1982; Reid *et al.* 1990; Ravat 1996; Nabighian and Hansen 2001; Hansen and Suciu 2002; Ravat *et al.* 2002; FitzGerald, Reid and McInerney 2004), the 2D analytic signal (Nabighian 1972, 1974) and the 3D total gradient techniques.

Gravity, magnetic field and gradient data are also applied to solid Earth studies, such as crustal structure (Behrendt, Meister and Henderson 1966; Thomas, Grieve and Sharpton 1988; Allen and Hinze 1992; Bosum *et al.* 1997; Cochran *et al.* 1999; Berrino, Corrado and Riccardi 2008), the

*E-mail: bingzhuw@gmail.com

lithosphere (Martinez, Goodliffe and Taylor 2001; Hebert *et al* 2001; Jallouli, Mickus and Turki 2002; Abers *et al.* 2002; Fischer 2002), continental rift studies (Martinez *et al* 2001; Abers *et al.* 2002; Mickus *et al.* 2007), impact structure (Ravat *et al.* 2002), geothermal models (Bektaş *et al.* 2007; Purucker *et al.* 2007), seismicity (Kostoglodov *et al.* 1996), bathymetry (Wang 2000) and volcanic island studies (Carbó *et al.* 2003; Blanco-Montenegro *et al.* 2005).

Potential, Potential Field (PF) and Potential-field Gradient (PG) data are supplemental to each other for resolving sources. Transformations facilitate data comparison and provide more means for interpretation by transforming the measured data into other forms of data. The fast Fourier transform (FT) is used widely in potential-field geophysics (e.g. Blakely 1996; Sandwell and Smith 1997; Mickus and Hinojosa 2001; Carbó *et al.* 2003). In theory, the Fourier transform techniques could be applied to perform potential-field transformations. However, the results of the Fourier transform techniques are often less accurate than one might like, and the Fourier transform techniques are only applied to regular grid points (e.g., Ricard and Blakely 1988; Wang 2006).

High-accuracy spline-based techniques of 3D and 2D potential-field upward continuation (Wang 2006) and potential field and gradient component transformations and derivative computations (Wang, Krebes and Ravat 2008) have been developed. In this paper, we propose flexible high-accuracy techniques to perform 3D and 2D integral transformations from PF components to potential and from PG components to PF components in the space domain with cubic B-splines. Using synthetic 3D gravity and magnetic transformation examples, we find that the spline techniques are substantially more accurate than the Fourier transform techniques, and demonstrate that harmonicity is confirmed substantially better for the spline method than the Fourier transform method and that spline-based integration and differentiation are invertible. Real data examples of 3D transformations show that the spline-based results agree substantially better (from gravity-gradient components to gravity) or better (between gravity-gradient components) with the observed data than do the Fourier-based results. For synthetic or real-data examples, relative root mean square errors between the computed values and the corresponding exact or observed values are taken to measure the accuracy.

POTENTIAL, POTENTIAL FIELD AND POTENTIAL-FIELD GRADIENT

Let $U(x, y, z)$ be the potential, $\mathbf{f}(x, y, z)$ be the potential field, and $\boldsymbol{D}(x, y, z)$ be the potential-field gradient tensor. For convenience, we use a uniform notation with $U(x, y, z)$ and its derivatives in this paper.

A potential field component equals to the corresponding partial derivative of the potential:

$$f_i(x, y, z) = U_i(x, y, z) = \frac{\partial U}{\partial i}, \quad i = x, y, z. \tag{1}$$

Analogously, a potential-field gradient component equals to the corresponding second-order partial derivative of the potential:

$$D_{ij}(x, y, z) = f_{ij}(x, y, z) = \frac{\partial f_i}{\partial j} = U_{ij}(x, y, z) = \frac{\partial^2 U}{\partial i \partial j}, \quad i, j = x, y, z. \tag{2}$$

Any potential field $\mathbf{f}(x, y, z)$ is conservative and curl free, i.e. $\nabla \times \mathbf{f}(x, y, z) = \mathbf{0}$, so that

$$U_{ji}(x, y, z) = U_{ij}(x, y, z), \quad i, j = x, y, z, \quad i \neq j. \tag{3}$$

In the region outside the sources any potential field $\mathbf{f}(x, y, z)$ is divergence free, i.e. $\nabla \cdot \mathbf{f}(x, y, z) = 0$. Therefore Laplace's equation holds

$$U_{zz}(x, y, z) = -[U_{xx}(x, y, z) + U_{yy}(x, y, z)]. \tag{4}$$

Considering equations (3) and (4), for the 3D case only five (e.g., $U_{xx}, U_{xy}, U_{xz}, U_{yy}, U_{yz}$) of the nine components of the gradient tensor $\boldsymbol{D}(x, y, z)$ are independent. Analogously, for the 2D case only two (e.g., U_{xx}, U_{xz}) of the four components of the gradient tensor $\boldsymbol{D}(x, z)$ are independent.

CALCULATING HORIZONTAL INDEFINITE INTEGRALS WITH CUBIC B-SPLINES

The 2D case

Approximate $V(x) = U_{xk}$, $k = x, z$ or $V(x) = U_x$ with splines, satisfying conditions (A7) and (A8). The interpolation coefficients $\{C_i\}$ can be determined (Appendix A). We then have

$$\int V(x)dx = \sum_{i=-1}^{N+1} C_i N_i^{-1}(x), \tag{5}$$

where $N_i^{-1}(x)$ is given by equation (A3) in Appendix A.

The 3D case

Approximate $V(x, y) = U_{xk}$, $k = x, y, z$ or $V(x, y) = U_x$ with splines, satisfying conditions (B3) through (B6). The interpolation coefficients $\{C_{i,j}\}$ can be determined (Appendix B). We

then have

$$\int V(x, y)dx = \sum_{i=-1}^{Nx+1} \sum_{j=-1}^{Ny+1} N_i^{-1}(x) C_{i,j} N_j(y). \quad (6)$$

Similarly, approximating $V(x, y) = U_{yk}$, $k = x, y, z$ or $V(x, y) = U_y$ with splines, satisfying conditions (B3) through (B6). We then have

$$\int V(x, y)dy = \sum_{i=-1}^{Nx+1} \sum_{j=-1}^{Ny+1} N_i(x) C_{i,j} N_j^{-1}(y), \quad (7)$$

where $N_i(x)$, $N_i^{-1}(x)$ are given by equation (A3) in Appendix A, and $N_j(y)$, $N_j^{-1}(y)$ are similarly obtained for subscript j.

TRANSFORMATIONS FROM PF COMPONENTS TO POTENTIAL

2D transformations from U_x to U

Let $V(x)$ be $U_x(x)$ and use equation (5) to obtain $U(x)$.

3D transformations from U_x or U_y to U

Let $V(x, y)$ be $U_x(x, y)$ or $U_y(x, y)$ and use equation (6) or (7) to obtain $U(x, y)$.

TRANSFORMATIONS FROM PG COMPONENTS TO PF COMPONENTS

2D transformations from U_{xx} to (U_x, U_z)

Let $V(x)$ be $U_{xx}(x)$ and use equation (5) to obtain $U_x(x)$. Knowing $U_x(x)$, calculate $U_z(\xi)$ (Wang *et al.* 2008) from

$$U_z(\xi) = \frac{1}{\pi} \int_{-\infty}^{\infty} \frac{U_x(x)}{\xi - x} dx. \quad (8)$$

2D transformations from U_{xz} to (U_x, U_z)

Let $V(x)$ be $U_{xz}(x)$ and use equations (5) to obtain $U_z(x)$. Knowing $U_z(x)$, $U_x(\xi)$ can be calculated (Wang *et al.* 2008) from

$$U_x(\xi) = -\frac{1}{\pi} \int_{-\infty}^{\infty} \frac{U_z(x)}{\xi - x} dx. \quad (9)$$

3D transformations from U_{xy} to (U_x, U_y, U_z)

Consider equations (6) and (7). Let $V(x, y)$ be $U_{xy}(x, y)$, then $U_x(x, y)$ and $U_y(x, y)$ can be calculated. Knowing $U_x(x, y)$ and $U_y(x, y)$, calculate $U_z(\xi, \eta)$ (Wang *et al.* 2008) from

$$U_z(\xi, \eta) = \frac{1}{2\pi} \int_{-\infty}^{\infty} \int_{-\infty}^{\infty} \frac{(\xi - x)U_x(x, y) + (\eta - y)U_y(x, y)}{[(x - \xi)^2 + (y - \eta)^2]^{3/2}} dxdy. \quad (10)$$

3D transformations from U_{xz} or U_{yz} to (U_x, U_y, U_z)

Let $V(x, y)$ be $U_{xz}(x, y)$ or $U_{yz}(x, y)$ and use equation (6) or (7) to obtain $U_z(x, y)$. Knowing $U_z(\xi, \eta)$, calculate $U_x(\xi, \eta)$ and $U_y(\xi, \eta)$ (Wang *et al.* 2008) from

$$U_x(\xi, \eta) = -\frac{1}{2\pi} \int_{-\infty}^{\infty} \int_{-\infty}^{\infty} \frac{(\xi - x)U_z(x, y)}{[(x - \xi)^2 + (y - \eta)^2]^{3/2}} dxdy, \quad (11)$$

$$U_y(\xi, \eta) = -\frac{1}{2\pi} \int_{-\infty}^{\infty} \int_{-\infty}^{\infty} \frac{(\eta - y)U_z(x, y)}{[(x - \xi)^2 + (y - \eta)^2]^{3/2}} dxdy. \quad (12)$$

3D transformations from (U_{xx}, U_{yy}) to (U_x, U_y, U_z)

Let $V(x, y)$ be $U_{xx}(x, y)$ and use equation (6) to obtain $U_x(x, y)$. Let $V(x, y)$ be $U_{yy}(x, y)$ and use equation (7) to obtain $U_y(x, y)$. Knowing $U_x(x, y)$ and $U_y(x, y)$, compute $U_z(\xi, \eta)$ using equation (10).

EVALUATION OF INFINITE INTEGRALS AND DOUBLE INTEGRALS

Equations (8 and 9) are similar infinite integral relations. When the computational domain $D_1 = \{x | a \le x \le b\}$ is well beyond the lateral extent of all sources of interest, approximate each infinite integral with a definite integral and evaluate it using the spline technique. To avoid a singularity, the sampling point (ξ) must not coincide with a spline knot (x). The centre of each interval of the spline grid is an ideal location for a sampling point. For a given point (ξ), approximate the whole of the integrand in equation (8), e.g., with splines, the interpolation coefficients $\{C_i\}$ can be determined (Appendix A). Thus, we have

$$U_z(\xi) = \frac{1}{\pi} \sum_{i=-1}^{N+1} C_i(\xi)[N_i^{-1}(b) - N_i^{-1}(a)], \quad (13)$$

where $N_i^{-1}(\cdot)$ is given by equation (A3) in Appendix A.

Equations (10 and 12) are similar infinite double integral relations. When the computational domain $D_2 = \{(x, y) | a \le x \le b,\ c \le y \le d\}$ is well beyond the lateral extent of all sources of interest, approximate each infinite double integral with a definite double integral and evaluate it using the spline technique. To avoid a singularity, the sampling point (ξ, η) must not coincide with a spline knot (x, y). The centre of each rectangular unit of the spline grid is an ideal location for a sampling point. For a given point (ξ, η), approximate the whole of the integrand in equation (10), e.g., with splines, the interpolation coefficients $\{C_{i,j}\}$ can be determined (Appendix

B). Thus, we have

$$U_z(\xi,\eta) = \frac{1}{2\pi}\sum_{i=-1}^{Nx+1}\sum_{j=-1}^{Ny+1}[N_i^{-1}(b) - N_i^{-1}(a)]C_{i,j}(\xi,\eta) \times [N_j^{-1}(d) - N_j^{-1}(c)], \quad (14)$$

where $N_i^{-1}(\cdot)$ is given by equation (A3) in Appendix A, and $N_j^{-1}(\cdot)$ is similarly obtained for subscript j.

SYNTHETIC EXAMPLES

3D gravity example of U_z obtained from noisy U_{xz} with the spline technique and comparison with the Fourier transform technique

In equation (6), let $V(x, y) = U_{xz}$, calculate U_z. The 3D sources are four solid spheres with densities and geometrical parameters listed in Table 1. Figure 1 shows the effectiveness of computing U_z from U_{xz} in the noisy situation. Figure 1(f) shows the U_{xz} data contaminated by random noise with a zero mean and a standard deviation of 0.65 mGal/km. Figure 1a shows the exact theoretical U_z map. The U_z map obtained using the spline technique is shown in Fig. 1(b). In order to improve the performance of both the spline technique and the Fourier transform technique, expand the original grids with 32 data points on each side of the computational domain and taper the expanded parts, but just keep the computed U_z values on the original grids. The U_z map obtained using the spline technique from the expanded U_{xz} data is shown in Fig. 1(c). The U_z map obtained using the Fourier transform technique is shown in Fig. 1(d). Fig. 1(e) shows the U_z map obtained using the Fourier transform technique from the expanded U_{xz} data.

In order to measure the difference between the computed values V_{ci} and the corresponding exact or observed values V_{ti}, define the RE (relative root mean square error) as

$$RE = \frac{\sqrt{\frac{1}{N}\sum_{i=1}^{N}(V_{ci} - V_{ti})^2}}{(V_{ti})_{\max} - (V_{ti})_{\min}}. \quad (15)$$

Table 1 Source parameters of the four solid spheres in Fig. 1. The centre of a sphere is at (x_0, y_0, z_0). The radius of the sphere is a and its density is ρ

Sphere	x_0(km)	y_0(km)	z_0(km)	a(km)	ρ(kg/m^3)
1	0.0	0.0	6.0	3.8	1200
2	10.0	0.0	1.6	1.5	1500
3	−5.0	8.7	1.6	1.5	1500
4	−5.0	−8.7	1.6	1.5	1500

Compared with Fig. 1(b), Fig. 1(d) is significantly less accurate. Compared with Fig. 1(c), Fig. 1(e) is significantly less accurate and based on Fig. 1(e) one can hardly identify the large source located at the centre. So, the results computed with the spline technique agree substantially better with the exact data than do the results computed with the Fourier transform technique. This statement is verified by comparing the REs shown in Table 2.

The pertinent computation times of this example with a 2.80 GHz laptop computer for different grid sizes and different methods are listed in Table 3. The extra time overhead of the spline method is the penalty for its increased accuracy.

Let the grid dimension be N, and the computation time be Y. For the spline method, $Y(N)=C_1(N)N^{2.9}$. For the Fourier transform method, $Y(N)=C_2(N)N^2\log_{10}N$. The boundedness of $C_1(N)$ and $C_2(N)$ (Table 3) suggests the polynomial $O(N^{2.9})$ growth for the spline method and the usual $O(N^2\ log_{10}N)$ growth for the Fourier transform method.

3D example of magnetic potential computed from a noisy x-component of magnetic induction with the spline technique and comparison with the Fourier transform technique

The 3D source is a solid sphere, whose magnetic and geometrical parameters are the following: inclination, declination and intensity of magnetization of the sphere are 60 degree, 20 degree and 1 *A/m*, respectively; the centre of the sphere is at (0, 0, 1.2 km) and the radius of the sphere is 0.5 km. Analytical magnetic potential (U_m) and x-component of magnetic induction (B_x) can be calculated (Blakely 1996). $U_m = -\frac{1}{\mu_0}\int B_x dx$ where μ_0 is permeability of free space. In equation (6), let $V(x,y) = B_x(x,y)$ and calculate U_m. Figure 2 shows the effectiveness of computing U_m from B_x in the noisy situation. The B_x data contaminated by random noise with a zero mean and a standard deviation of 0.5 nT are shown in Fig. 2(f). Figure 2(a) shows the exact theoretical U_m map. The U_m map obtained using the spline technique is shown in Fig. 2(b). In order to improve the performance of both the spline technique and the Fourier transform technique, expand the original grids with 32 data points on each side of the computational domain and taper the expanded parts, but only keep the computed U_m values on the original grids. The U_m map obtained using the spline technique from the expanded B_x data is shown in Fig. 2(c). Figure 2(d) shows the U_m map obtained using the Fourier transform technique. The U_m map obtained using the Fourier transform technique from the expanded B_x data is shown in Fig. 2(e). Compared with Fig. 2(b), Fig. 2(d) is significantly less accurate. So is Fig. 2(e), compared with

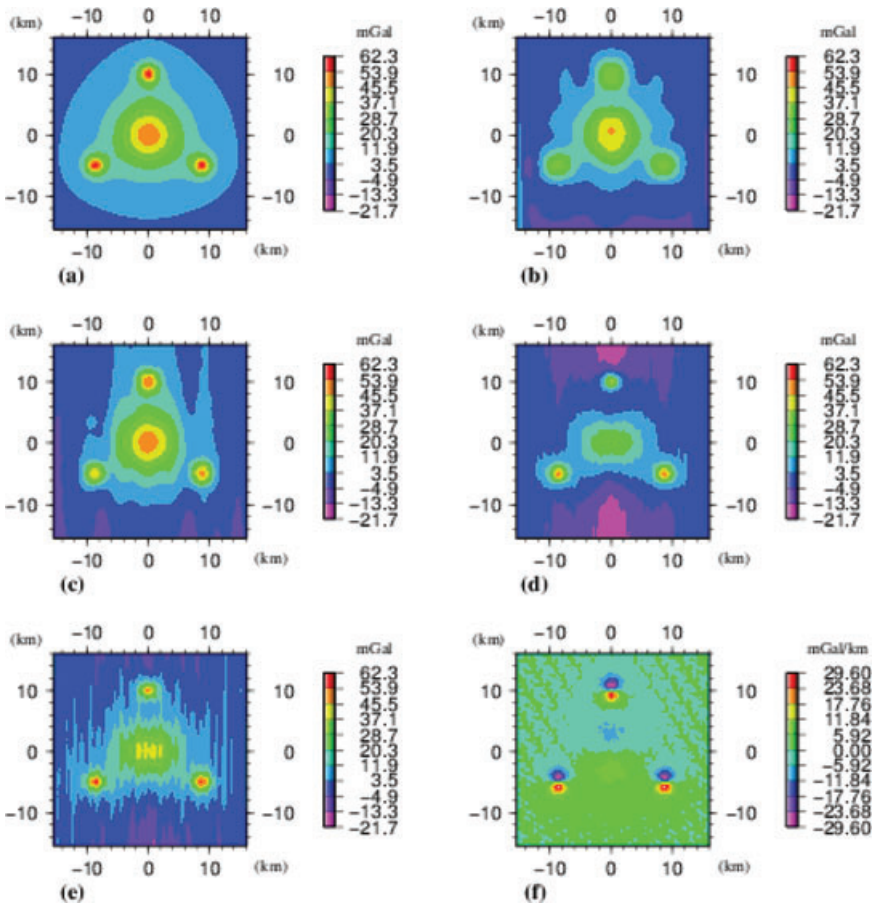

Figure 1 The 3D gravity example of U_z obtained from noisy U_{xz} data using the spline technique and the Fourier transform technique. The sources are four solid spheres with densities and geometrical parameters listed in Table 1. Data spacing is 0.5 km in both the x and y directions. (a) U_z (analytical). (b) U_z from U_{xz} (spline). (c) U_z from expanded U_{xz}(spline). (d) U_z from U_{xz} (FT). (e) U_z from expanded U_{xz} (FT). (f) Noisy U_{xz} (contaminated by random noise with a zero mean and a standard deviation of 0.65 mGal/km).

Fig. 2(c). Therefore, the results computed with the spline technique agree substantially better with the exact data than do the results computed with the Fourier transform technique. The REs shown in Table 4 strongly support this statement.

3D gravity example of U_{xz} obtained from rectangular-gridded U_{zz} with the spline technique

This is a 3D gravity example of U_{xz} recovered from exact and noisy rectangular-gridded U_{zz} data using the spline technique (Wang *et al.* 2008). The 3D sources are five solid spheres with densities and geometrical parameters listed in Table 5. The data spacing is 0.15 km in the x direction and 0.10 km in the y direction. Figure 3(d) shows the exact theoretical U_{zz} data. The U_{xz} map obtained using the spline technique from the exact U_{zz} data is shown in Fig. 3(b). Figure 3(e) shows the U_{zz} data contaminated by random noise with a zero mean and a standard deviation of 0.41 mGal/km. The U_{xz} map obtained using the spline technique from the noisy U_{zz} data is shown in Fig. 3(c). Compared with the exact U_{xz} (Fig. 3a), the REs are 0.37% and 0.62% for the exact and noisy cases in Fig. 3(b, c), respectively.

Table 2 REs between panels I, I = (b), (c), (d), (e) and panel (a) in Fig. 1

Panel	(b)	(c)	(d)	(e)
RE (%)9	8.72	7.29	19.13	10.29

REAL DATA EXAMPLES

The real data are the free air gravity and full tensor gravity gradient dataset (U_z and U_{xx}, U_{xy}, U_{xz}, U_{yy}, U_{yz}, U_{zz})

Table 3 Time complexity of the spline and Fourier transform methods

N ($N \times N$ grid)	t_{spline} (second)	t_{FT} (second)	t_{spline} ($N^{2.9}$)	t_{FT} ($N^2 log_{10} N$)
64	0.656	0.031	3.79e-06	4.19e-06
128	4.672	0.141	3.62e-06	4.08e-06
256	36.55	0.563	3.79e-06	3.57e-06

collected in the Gulf of Mexico. The dataset satisfies equation (4) (Laplace's equation) well. Using the spline-based techniques, the following transformations are performed.

3D gravity-gradient component transformations

Examples of these are shown in Fig. 4. The computed U_{zz} recovered from the observed U_{xz} and U_{yz} (Fig. 5b) data using the spline technique (Wang *et al.* 2008) and the Fourier transform technique are shown in Fig. 4(b) and 4(c), respectively. Compared with the observed U_{zz} data (Fig. 4a), the RE is 6.89% for the spline technique and 14.86% for the Fourier transform technique.

Figures 4(e,f) show the computed U_{xz} recovered from the observed U_{zz} data using the spline technique and the Fourier transform technique, respectively. Compared with the

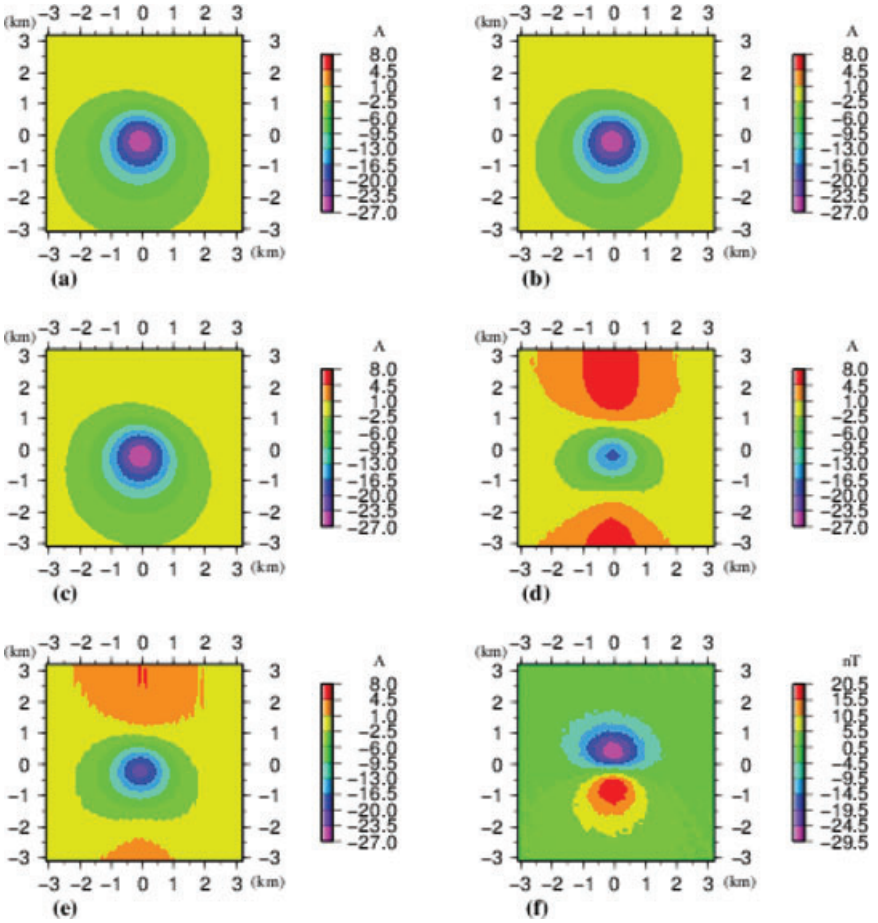

Figure 2 The 3D magnetic example of U_m obtained from noisy B_x data using the spline technique and the Fourier transform technique. The source is a solid sphere centered at (0, 0, 1.2 km) with a radius of 0.5 km. Data spacing is 0.1 km in both the x and y directions. (a) U_m(analytical). (b) U_m from B_x (spline). (c) U_m from expanded B_x (spline). (d) U_m from B_x (FT). (e) U_m from expanded B_x (FT). (f) Noisy B_x (contaminated by random noise with a zero mean and a standard deviation of 0.5 nT).

Table 4 REs between panels I, I = (b), (c), (d), (e) and panel (a) in Fig. 2

Panel	(b)	(c)	(d)	(e)
RE (%)	1.43	1.37	17.34	10.23

Table 5 Source parameters of the five solid spheres in Figs. 3, 6, 7, 8 and 9. The centre of a sphere is at (x_0, y_0, z_0). The radius of the sphere is a, and its density is ρ

Sphere	x_0(km)	y_0(km)	z_0(km)	a(km)	ρ(kg/m^3)
1	0.0	0.0	1.72	1.56	1000
2	1.2	1.2	0.6	0.5	1000
3	−1.5	1.5	0.6	0.5	1000
4	−1.2	−1.2	0.6	0.5	1000
5	1.5	−1.5	0.6	0.5	1000

observed U_{xz} data (Fig. 4d), the RE is 10.45% for the spline technique and 10.57% for the Fourier transform technique.

The computed U_{xy} recovered from the observed U_{xz} data with the spline technique and the Fourier transform technique are shown in Figs. 4(h, i), respectively. Compared with the observed U_{xy} data (Fig. 4g), the RE is 9.41% for the spline technique and 12.40% for the Fourier transform technique.

The results computed with the spline technique agree better with the observed data than do the results computed with the Fourier transform technique, although the differences in this example are not as pronounced as in other cases, e.g., between Figs. 2(c) and 2(e), or Figs. 5(g) and 5(h).

3D gravity U_z obtained from gravity-gradient components U_{xz} and U_{yz}

An example is shown in Fig. 5. Figure 5(b) shows the observed U_{yz} data. The observed U_{xz} data are shown in Fig. 4(d).

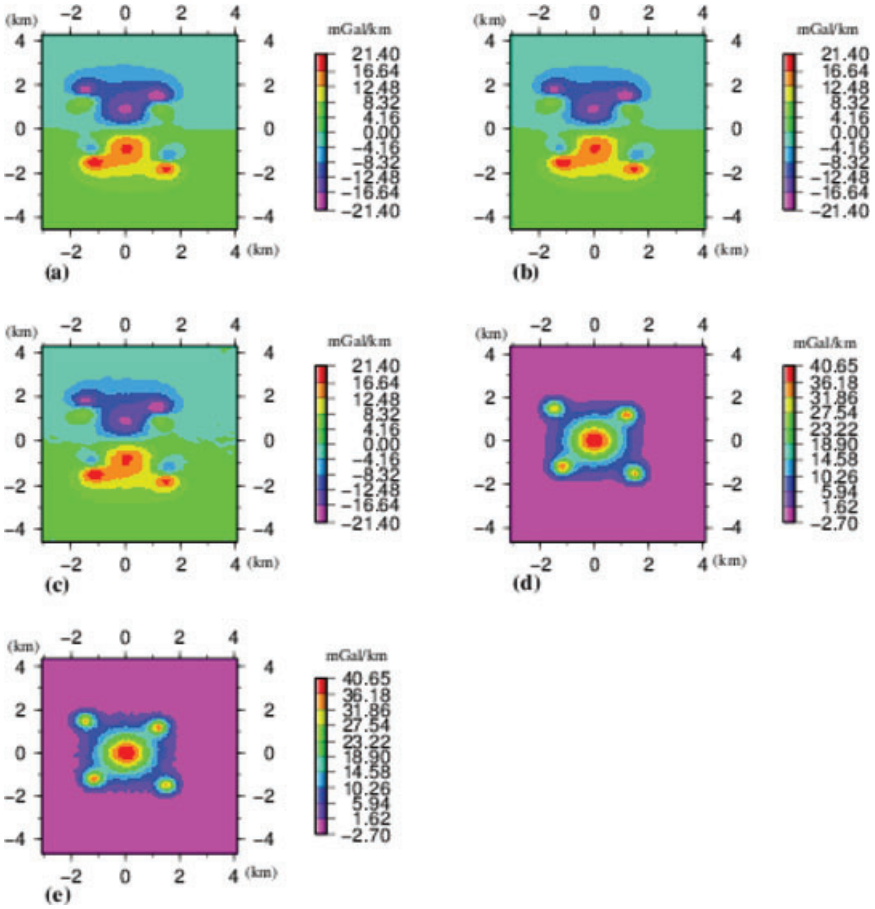

Figure 3 The 3D gravity example of U_{xz} obtained from exact and noisy rectangular-gridded U_{zz} data using the spline technique. The sources are five solid spheres with densities and geometrical parameters listed in Table 5. Data spacing is 0.15 km in the x direction and 0.10 km in the y direction. (a) U_{xz} (analytical). (b) U_{xz} from exact U_{zz}. (c) U_{xz} from noisy U_{zz}. (d) U_{zz} (analytical). (e) Noisy U_{zz} (contaminated by random noise with a zero mean and a standard deviation of 0.41 mGal/km).

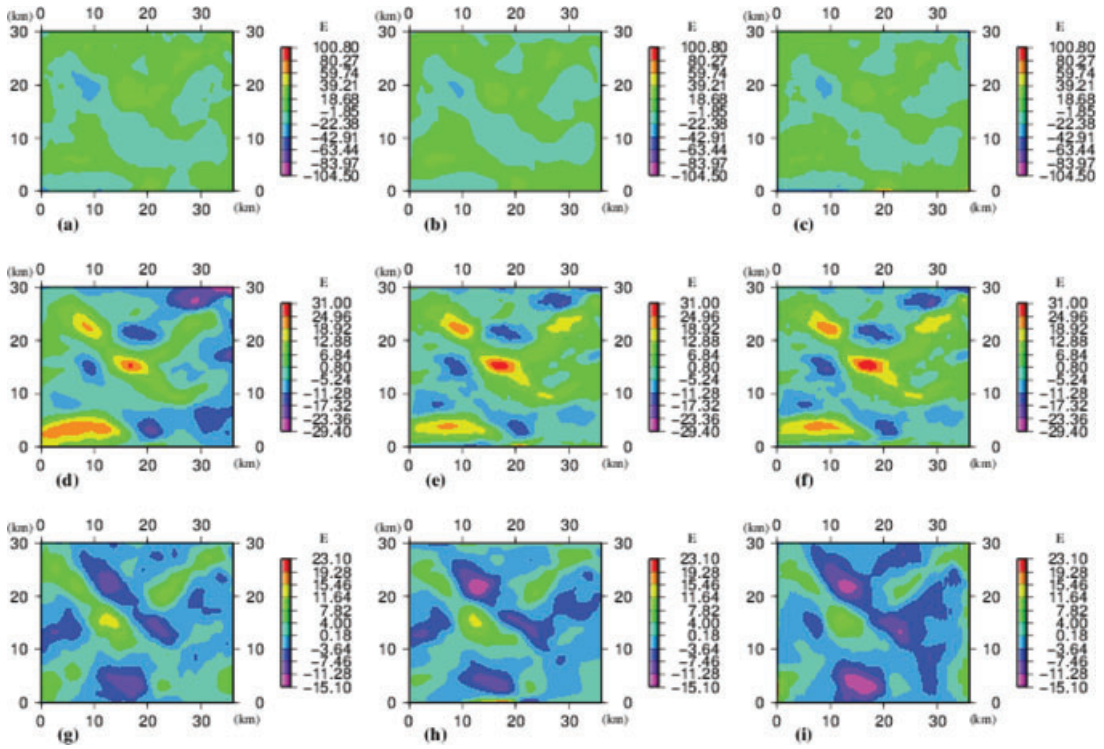

Figure 4 Real 3D examples of gravity-gradient component transformations. The data were collected in the Gulf of Mexico with data spacing of 0.5 km in both the x and y directions. (a) U_{zz}(observed). (b) U_{zz} from observed U_{xz} and U_{yz} (spline). (c) U_{zz} from observed U_{xz} and U_{yz} (FT). (d) U_{xz} (observed). See the observed U_{yz} data in Fig. 5(b). (e) U_{xz} from observed U_{zz} (spline). (f) U_{xz} from observed U_{zz} (FT). (g) U_{xy} (observed). (h) U_{xy} from observed U_{xz} (spline). (i) U_{xy} from observed U_{xz} (FT).

In equation (6), let $V(x,y)=U_{xz}$ and calculate gravity $\boldsymbol{U}_z$. In equation (7), let $V(x,y) = U_{yz}$ and calculate $\boldsymbol{U}_z$ again. Figures 5(c, d) are the computed $\boldsymbol{U}_z$ obtained from $\boldsymbol{U}_{yz}$ with the spline technique and the Fourier transform technique, respectively. Figures 5(e, f) are the computed $\boldsymbol{U}_z$ obtained from $\boldsymbol{U}_{xz}$ with the spline technique and the Fourier transform technique, respectively. Figure 5(g) shows the computed $\boldsymbol{U}_z$ with the spline technique averaged from panels (c) and (e). The computed $\boldsymbol{U}_z$ with the Fourier transform technique averaged from panels (d) and (f) is shown in Fig. 5(h). Compared with the observed $\boldsymbol{U}_z$ data (Fig. 5a), the REs are: (c) 15.07%, (d) 63.51%, (e) 23.25%, (f) 79.27%, (g) 12.01%, (h) 65.34%.

Apparently, the results computed with the spline technique agree substantially better with the observed $\boldsymbol{U}_z$ data than do the results computed with the Fourier transform technique.

HARMONICITY AND INVERTIBILITY TESTS

Harmonicity test using computed U_{xx}, U_{yy} and analytical U_{zz}

This is a 3D gravity example of harmonicity confirmation for the spline technique. The sources are five solid spheres with densities and geometrical parameters listed in Table 5. Data spacing is 0.05 km in both the x and y directions. There are three steps:

(I) compute potential $\boldsymbol{U}$ from the forwarded potential field $\boldsymbol{U}_x$; compute the first-order partial derivative $\tilde{U}_x$ from the potential $\boldsymbol{U}$; then compute the second-order partial derivative $\boldsymbol{U}_{xx}$ from the $\tilde{U}_x$.

(II) compute potential $\boldsymbol{U}$ from the forwarded potential field $\boldsymbol{U}_y$; compute the first-order partial derivative $\tilde{U}_y$ from the potential $\boldsymbol{U}$; then compute the second-order partial derivative $\boldsymbol{U}_{yy}$ from the $\tilde{U}_y$.

(III) sum up the exact theoretical $\boldsymbol{U}_{zz}$ and the $\boldsymbol{U}_{xx}$ and $\boldsymbol{U}_{yy}$ calculated in (I) and (II).

Define the norm of an array of values V_i:

$$Norm = \frac{1}{N}\sqrt{\sum_{i=1}^{N}(V_i)^2}. \tag{16}$$

Steps (I), (II) and (III) apply to both the spline technique and the Fourier transform technique. Figures 6(a) and 6(d) are analytical U_{xx} and U_{yy}, respectively. The spline-based U_{xx} (Fig. 6b) and U_{yy} (Fig. 6e) agree substantially better with the

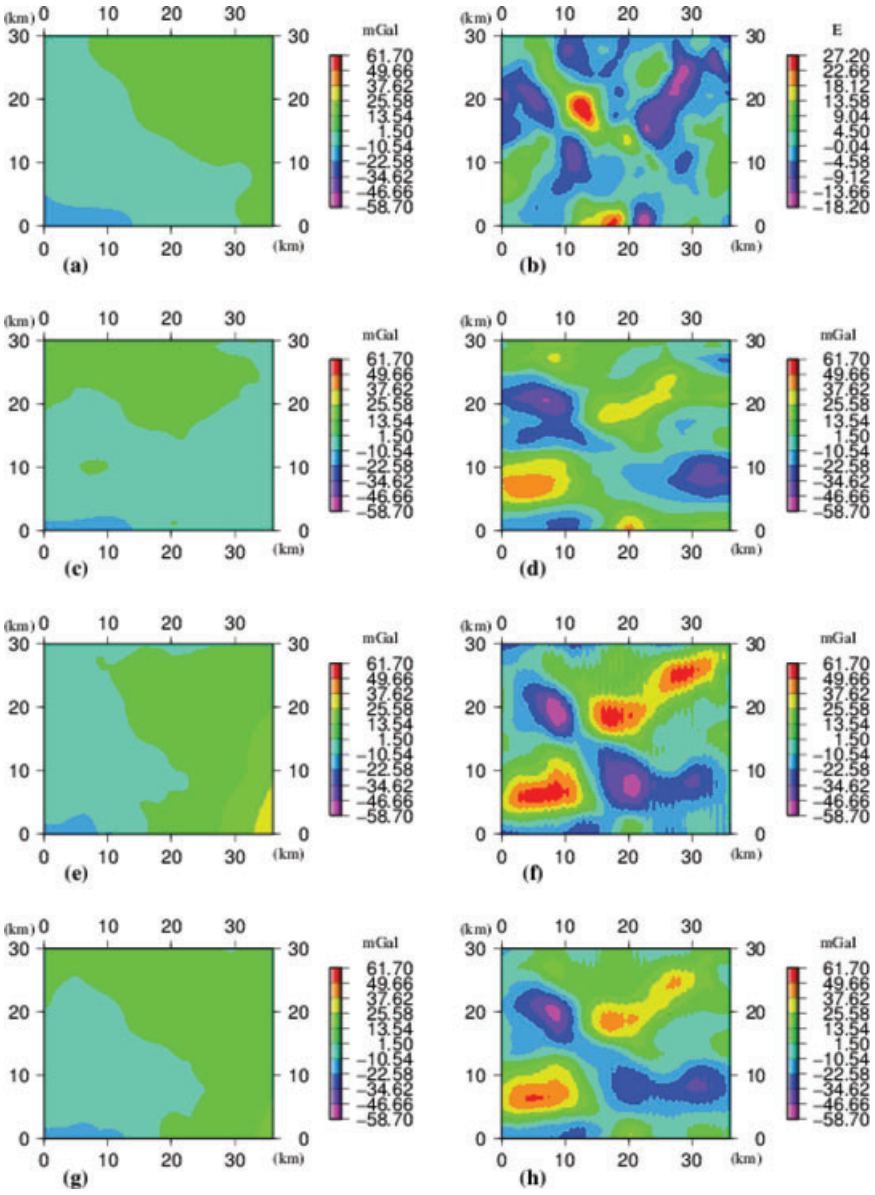

Figure 5 Real 3D example of gravity U_z obtained from gravity-gradient components U_{xz} and U_{yz}. The data were collected in the Gulf of Mexico with data spacing of 0.5 km in both the x and y directions. (a) U_z (observed). (b) U_{yz} (observed). The observed U_{xz} data are in Fig. 4(d). (c) U_z from U_{yz} (spline). (d) U_z from U_{yz} (FT). (e) U_z from U_{xz} (spline). (f) U_z from U_{xz} (FT). (g) U_z (spline), averaged from panels (c) and (e). (h) U_z (FT), averaged from panels (d) and (f).

analytical results than do the Fourier transform-based U_{xx} (Fig. 6c) and $\boldsymbol{U}_{yy}$ (Fig. 6f).

The sum of Figs. 6(a), 6(d) and 6(g) (analytical U_{zz}), the exact theoretical second-order derivatives, is exactly zero everywhere, perfectly satisfying Laplace's equation. The sum of Figs. 6(b), 6(e) and 6(g), shown in Fig. 6(h) (*Norm* 0.002 mGal/km), is nearly zero, almost perfectly satisfying Laplace's equation, which confirms harmonicity for the spline technique. The U_{xx} and U_{yy} are so accurately calculated with the spline technique, U_{zz} can be reliably obtained using the Laplace's equation (equation 4). Interestingly, one can identify the four shallow sources shown as distinct anomalies on Fig. 6(h).

The sum of Figs. 6(c), 6(f) and 6(g), shown in Fig. 6(i) (norm 0.302 mGal/km), is not nearly as close to zero as the sum in Fig. 6(h). i.e., harmonicity is substantially less well confirmed

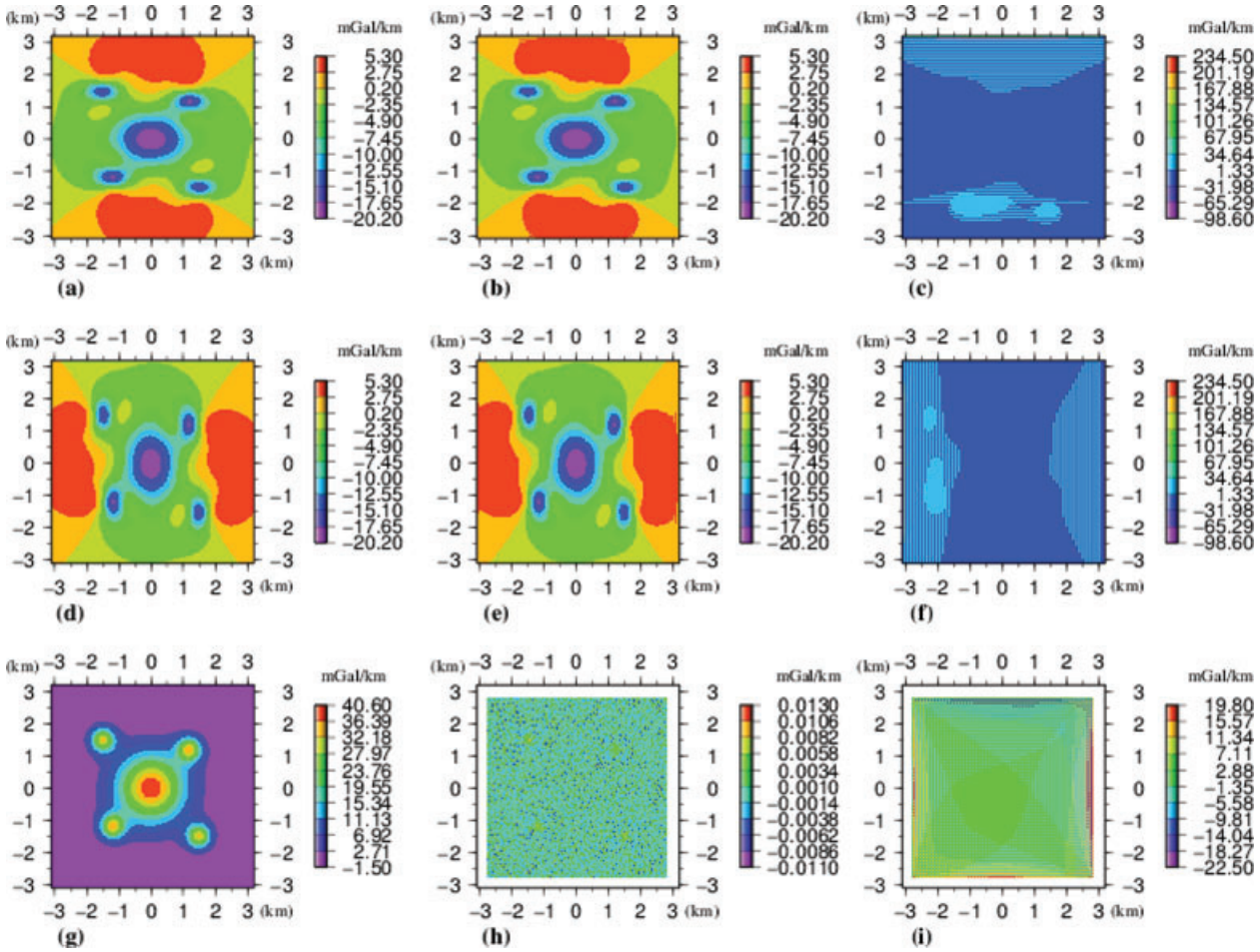

Figure 6 3D gravity example of harmonicity confirmation for the spline technique and comparison with the Fourier transform technique. U_{xx} and U_{yy} are computed, U_{zz} is analytical. The sources are five solid spheres with densities and geometrical parameters listed in Table 5. Data spacing is 0.05 km in both the x and y directions. (a) U_{xx} (analytical). (b) U_{xx} (spline). (c) U_{xx} (FT). (d) U_{yy} (analytical). (e) U_{yy} (spline). (f) U_{yy} (FT). (g) U_{zz} (analytical). (h) U_{xx}(spline) + U_{yy}(spline) + U_{zz}(analytical). (i) U_{xx}(FT) + U_{yy}(FT) + U_{zz}(analytical).

for the Fourier transform method than the spline method. Both methods have some edge effects. However, the edge problem is significantly less severe for the spline technique than the Fourier transform technique.

Harmonicity tests using computed U_{xx}, U_{yy}, U_{zz}

These are further harmonicity tests for the spline technique and the Fourier transform technique. The sources are five solid spheres with densities and geometrical parameters listed in Table 5. Data spacing is 0.1 km in both the x and y directions. The following describes the procedure.

(I) Compute potential $\boldsymbol{U}$ from the forwarded potential field $\boldsymbol{U}_x$; compute the first-order partial derivative $\tilde{U}_x$ from the potential $\boldsymbol{U}$; then compute the second-order partial derivative $\boldsymbol{U}_{xx}$ from the $\tilde{U}_x$.

(II) Compute potential $\boldsymbol{U}$ from the forwarded potential field $\boldsymbol{U}_y$; compute the first-order partial derivative $\tilde{U}_y$ from the potential $\boldsymbol{U}$; then compute the second-order partial derivative $\boldsymbol{U}_{yy}$ from the $\tilde{U}_y$.

(III) It takes the following steps to compute $\boldsymbol{U}_{zz}$: Compute $\boldsymbol{U}_{xy}$ from the $\tilde{U}_x$ obtained in (I), and compute $\boldsymbol{U}_{yx}$ from the $\tilde{U}_y$ obtained in (II); compute $\boldsymbol{U}_{xz}$ from $\boldsymbol{U}_{xy}$ and $\boldsymbol{U}_{xx}$ obtained in (I); compute $\boldsymbol{U}_{yz}$ from $\boldsymbol{U}_{yx}$ and $\boldsymbol{U}_{yy}$ obtained in (II); compute $\boldsymbol{U}_{zz}$ from $\boldsymbol{U}_{xz}$ and $\boldsymbol{U}_{yz}$.

(IV) Sum up the $\boldsymbol{U}_{xx}$, $\boldsymbol{U}_{yy}$ and $\boldsymbol{U}_{zz}$ calculated in (I), (II) and (III).

(I), (II), (III) and (IV) apply to both the spline technique and the Fourier transform technique. Figures 7(h, i) are the U_{xy} maps computed with the spline technique and the Fourier transform technique, respectively. Both are very close to

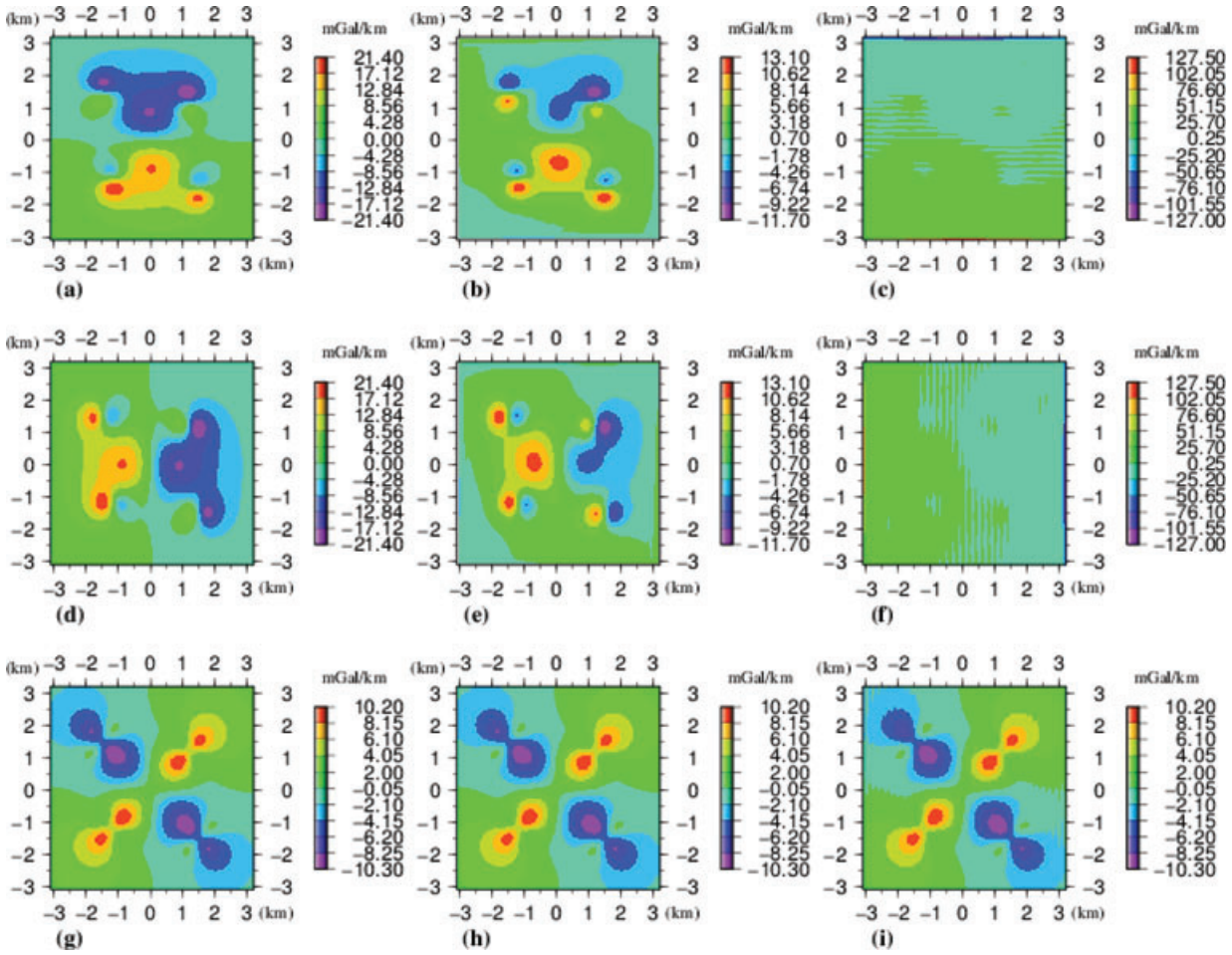

Figure 7 Intermediate steps of computing U_{zz} (Fig. 8): 3D gravity example to compare the spline technique and the Fourier transform technique for computing U_{xz}, U_{yz}, U_{xy}. The sources are five solid spheres with densities and geometrical parameters listed in Table 5. Data spacing is 0.1 km in both the x and y directions. (a) U_{xz} (analytical). (b) U_{xz} (spline). (c) U_{xz} (FT). (d) U_{yz} (analytical). (e) U_{yz} (spline). (f) U_{yz} (FT). (g) U_{xy} (analytical). (h) U_{xy} (spline). (i) U_{xy} (FT).

analytical U_{xy} as shown in Fig. 7(g). However, comparing with analytical U_{xz} (Fig. 7a) and U_{yz} (Fig. 7d), the spline-based U_{xz} (Fig. 7b) and U_{yz} (Fig. 7e) are obviously substantially better than the Fourier transform-based U_{xz} (Fig. 7c) and U_{yz} (Fig. 7f). Figures 8(a, b) are the U_{zz} maps and Figures 8(d, e) are the $U_{xx} + U_{yy} + U_{zz}$ maps obtained using the spline technique and the Fourier transform technique, respectively.

(V) There is another alternative way to compute $\boldsymbol{U}_{zz}$ using the Fourier transform technique: compute $\boldsymbol{U}_z$ from the $\boldsymbol{U}$ obtained in (I); then compute $\boldsymbol{U}_{zz}$ from $\boldsymbol{U}_z$. Figure 8f is the Fourier transform-based $\boldsymbol{U}_{xx} + \boldsymbol{U}_{yy} + \boldsymbol{U}_{zz}$ map, where $\boldsymbol{U}_{zz}$ (Fig. 8c) is the $\boldsymbol{U}_{zz}$ map computed through the alternative way using the Fourier transform technique. Apparently, this alternative approach is impractical to compute $\boldsymbol{U}_{zz}$ using the Fourier transform technique.

The norms (equation 16) for Figs. 8(d, e, f) are 0.144, 0.507, 165.232 mGal/km, respectively. i.e., harmonicity is again substantially less well confirmed for the Fourier transform method than the spline method.

Invertibility test

This is a 3D gravity example to test the invertibility of spline-based integration and differentiation. The sources are five solid spheres with densities and geometrical parameters listed in Table 5. Data spacing is 0.1 km in both the x and y directions. Figure 9(d) shows the exact theoretical $\boldsymbol{U}_x$ data. The $\boldsymbol{U}$ map obtained from the exact $\boldsymbol{U}_x$ data using the spline-based integration is shown in Fig. 9(b); compared with the exact $\boldsymbol{U}$ (Fig. 9a), the RE is 5.99%. Figure 9(c) shows the $\boldsymbol{U}_x$ map

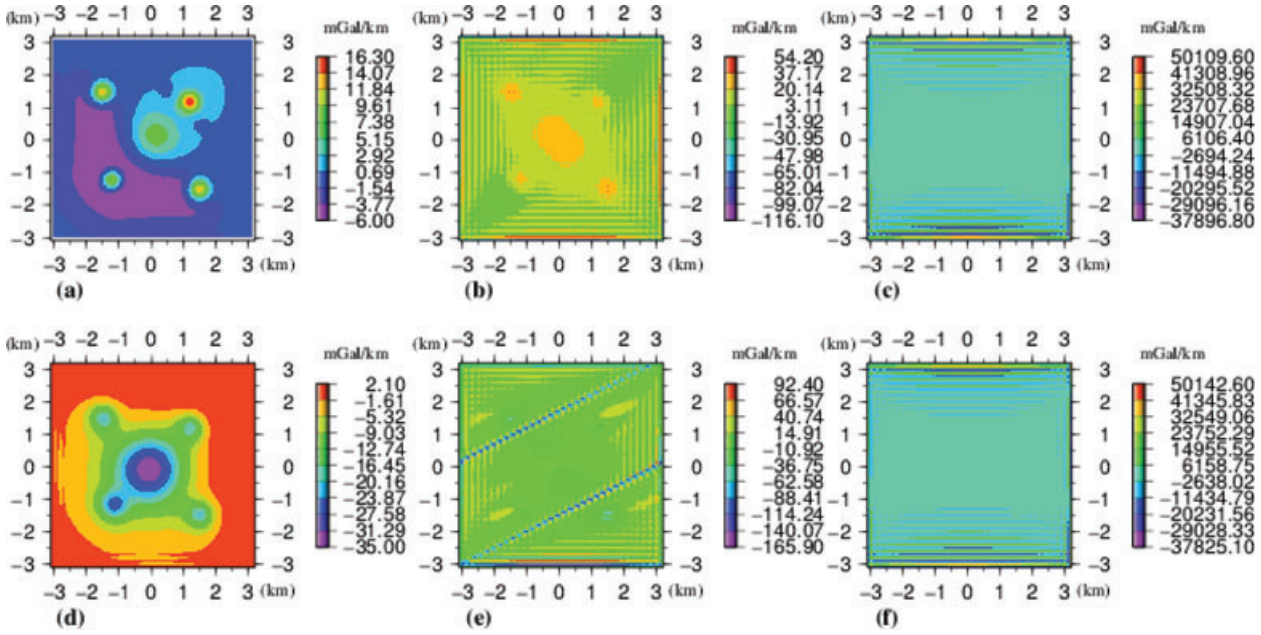

Figure 8 3D gravity example to test harmonicity of the spline technique and comparison with the FT technique, U_{xx}(Fig. 6), U_{yy}(Fig. 6), U_{zz} are all computed. The sources are five solid spheres with densities and geometrical parameters listed in Table 5. Data spacing is 0.1 km in both the x and y directions. (a) U_{zz} (spline). (b) U_{zz} (FT). (c) U_{zz} (alternative FT). (d) $U_{xx} + U_{yy}+U_{zz}$ (spline). (e) $U_{xx} + U_{yy} + U_{zz}$ (FT; U_{zz} panel b). (f) $U_{xx} + U_{yy} + U_{zz}$ (FT; U_{zz} panel c).

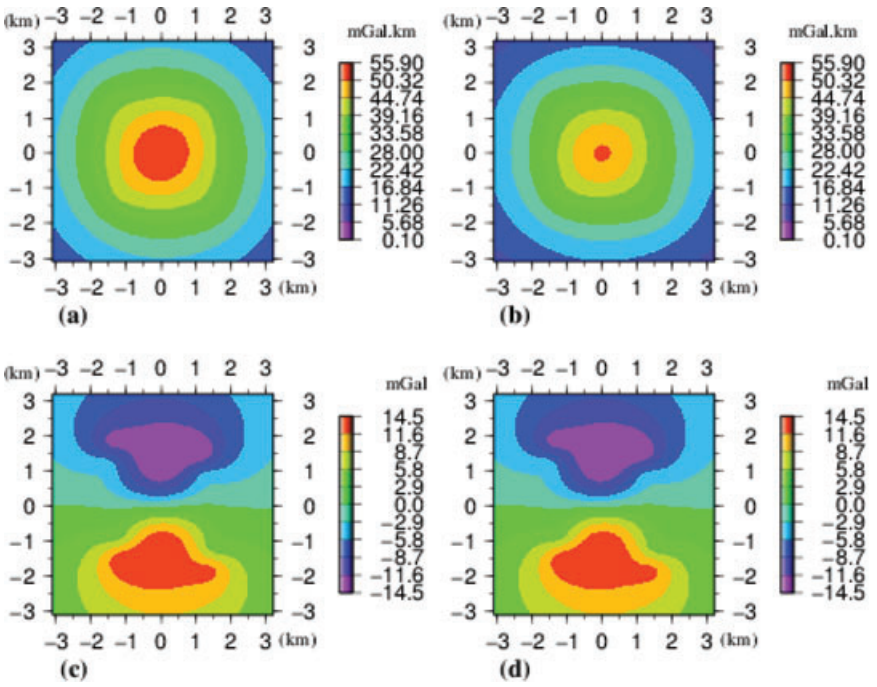

Figure 9. 3D gravity example to test whether spline-based integration and differentiation are invertible. The sources are five solid spheres with densities and geometrical parameters listed in Table 5. Data spacing is 0.1 km in both the x and y directions. (a) U (analytical). (b) U obtained from analytical U_x using spline-based integration. (c) U_x obtained from U in panel (b) using spline-based differentiation. (d) U_x (analytical).

obtained from the $\boldsymbol{U}$ as shown in Fig. 9(b) using the spline-based differentiation; compared with the exact $\boldsymbol{U}_x$(Fig. 9d), the RE is only 0.01%.

We have obtained the potential from the field and recovered the field from the computed potential nicely, so that spline-based integration and differentiation are invertible.

CONCLUSIONS

Potential, potential field and potential-field gradient data are supplemental to each other for resolving sources of interest. We advanced spline-based techniques for 3D and 2D potential-field upward continuation and potential field and gradient component transformations and derivative computations in the previous studies. In this paper, we propose flexible high-accuracy practical techniques to perform 3D and 2D integral transformations from PF components to potential and from PG components to PF components in the space domain using cubic B-splines. The spline techniques are applicable to either uniform or non-uniform rectangular grids for the 3D case, and applicable to either regular or irregular grids for the 2D case. The spline-based indefinite integrations can be computed at any point in the computational domain, as can the horizontal derivatives.

In our synthetic 3D gravity examples (U_z obtained from noisy U_{xz}, U_{xz} obtained from rectangular-gridded U_{zz}, and the demonstration that harmonicity is confirmed substantially better for the spline technique than the Fourier transform technique and spline-based integration and differentiation are invertible) and magnetic examples (U_m obtained from noisy B_x), we have shown that the spline techniques are substantially more accurate and hence may provide better insights into understanding the sources than the Fourier transform techniques, and U_{zz} can be reliably obtained using the Laplace's equation since the U_{xx} and U_{yy} are very accurately calculated with the spline technique. The cost of the increase in accuracy is some increase in computing time compared to the Fourier transform technique. However, the speed is still fast, e.g., the spline-based computation of U_z from U_{xz} on a 128 by 128 grid was performed within 5 seconds with a 2.80 GHz laptop computer. For the 3D gravity U_z obtained from U_{xz} example, the complexities of the computational time growth are polynomial $O(N^{2.9})$ growth for the spline method and the usual $O(N^2\ log_{10}N)$ growth for the Fourier transform method.

Our real data examples of 3D transformations show that the spline-based results agree substantially better (from gravity-gradient components to gravity) or better (between gravity-gradient components) with the observed data than do the Fourier-based results.

The spline techniques would therefore be very useful for data quality control through comparisons of the computed and observed components. If certain desired components of the potential field or gradient data are not measured, they can be obtained using the spline-based transformations as alternatives to the Fourier transform techniques.

ACKNOWLEDGEMENTS

We are grateful to editor Dr. Alan Reid, the associate editor and the reviewers for their very thoughtful and constructive comments and suggestions. This work was partially supported by the United States National Science Foundation awards EAR-0739015 and EAR-0952064 and a grant from the Natural Sciences and Engineering Research Council of Canada held by E.S. Krebes. We appreciate that John Mims provided the real gravity gradient data. Map plotting was facilitated with the use of GMT software (Wessel and Smith 1995). This article is Geology and Geophysics contribution 39 of Missouri University of Science and Technology.

REFERENCES

Abers G.A., Ferris A., Craig M., Davies H., Lerner-Lam A.L., Mutter J.C. and Taylor B. 2002. Mantle compensation of active metamorphic core complexes at Woodlark rift in Papua New Guinea. *Nature* **418**, 862–865.

Allen D.J. and Hinze W.J. 1992. Wisconsin gravity minimum: Solution of a geologic and geophysical puzzle and implications for cratonic evolution. *Geology* **20**, 515–518.

Behrendt J.C., Meister L. and Henderson J.R. 1966. Airborne geophysical study in the Pensacola Mountains of Antarctica. *Science* **153**, 1373–1376.

Bektaş O., Ravat D., Büyüksaraç A., Bİlİm F. and Ateş A. 2007. Regional geothermal characterisation of east Anatolia from aeromagnetic, heat flow and gravity data. *Pure Applied Geophysics* **164**, 975–998.

Berrino G., Corrado G. and Riccardi U. 2008. Sea gravity data in the Gulf of Naples. A contribution to delineating the structural pattern of the Phlegraean Volcanic District. *Journal of Volcanology and Geothermal Research* **175**, 241–252.

Blakely R.J. 1996. *Potential theory in gravity and magnetic applications*. Cambridge University Press.

Blakely R.J. and Simpson R.W. 1986. Approximating edges of source bodies from magnetic or gravity anomalies. *Geophysics* **51**, 1494–1498.

Blanco-Montenegro I., Gonzalez F.M., Garcia A., Vieira R. and Villalain J.J. 2005. Paleomagnetic determinations on Lanzarote from magnetic and gravity anomalies: Implications for the early history

of the Canary Islands. *Journal of Geophysical Research* **110**, B1 2102, 1–9.

Bosum W., Casten U., Fieberg F.C., Heyde I. and Soffel H.C. 1997. Three-dimensional interpretation of the KTB gravity and magnetic anomalies. *Journal of Geophysical Research* **102**(B8), 18307–18321.

Bracewell R.N. 1965. *The Fourier transform and its applications*. McGraw-Hill Inc.

Carbó A., Muñoz-MartÍn A., Llanes P., Álvarez J. and EEZ Working Group. 2003. Gravity analysis offshore the Canary Islands from a systematic survey. *Marine Geophysical Research* **24**, 113–127.

Cochran J.R., Fornari D.J., Coakley B.J., Herr R. and Tivey M.A. 1999. Continuous near-bottom gravity measurements made with a BGM-3 gravimeter in DSV Alvin on the East Pacific Rise crest near 9°3 1′N and 9°50′N. *Journal of Geophysical Research* **104**(B5), 10841–10861.

Fischer K.M. 2002. Waning buoyancy in the crustal roots of old mountains. *Nature* **417**, 933–936.

FitzGerald D., Reid A. and McInerney P. 2004. New discrimination techniques for Euler deconvolution. *Computers & Geosciences* **30**, 461–469.

Grauch V.J.S. and Cordell L. 1987. Limitations of determining density or magnetic boundaries from the horizontal gradient of gravity or pseudogravity data. *Geophysics* **52**, 118–121.

Hansen R.O. and Suciu L. 2002. Multiple-source Euler deconvolution. *Geophysics* **67**, 525–535.

Hebert H., Deplus C., Huchon P., Khanbari K. and Audin L. 2001. Lithospheric structure of a nascent spreading ridge inferred from gravity data: The western Gulf of Aden. *Journal of Geophysical Research* **106**(B11), 26345–26363.

Jallouli C., Mickus K.L. and Turki M.M. 2002. Gravity constrains on the structure of the northern margin of Tunisia: Implications on the nature of the northern African Plate boundary. *Geophysical Journal International* **151**, 117–131.

Kostoglodo V., Bandy W., Dominguez J. and Mena M. 1996. Gravity and seismicity over the Guerrero seismic gap, Mexico. *Geophysical Research Letters* **23**, 3385–3388.

Martinez F., Goodliffe A.M. and Taylor B. 2001. Metamorphic core complex formation by density inversion and lower-crust extrusion. *Nature* **411**, 930–934.

Mickus K.L. and Hinojosa J.H. 2001. The complete gravity gradient tensor derived from the vertical component of gravity: A Fourier transform technique. *Journal of Applied Geophysics* **46**, 159–174.

Mickus K., Tadesse K., Keller G.R. and Oluma B. 2007. Gravity analysis of the main Ethiopian rift. *Journal of African Earth Sciences* **48**, 59–69.

Nabighian M.N. 1972. The analytic signal of two-dimensional magnetic bodies with polygonal cross-section: Its properties and use for automated anomaly interpretation. *Geophysics* **37**, 507–517.

Nabighian M.N. 1974. Additional comments on the analytic signal with two-dimensional magnetic bodies with polygonal cross-section. *Geophysics* **39**, 85–92.

Nabighian M.N. 1984. Toward a three-dimensional automatic interpretation of potential field data via generalized Hilbert transforms: Fundamental relations. *Geophysics* **49**, 780–786.

Nabighian M.N., Ander M.E., Grauch V.J.S., Hansen R.O., LaFehr T.R., Li Y. *et al*. 2005b. Historical development of the gravity method in exploration. *Geophysics* **70**, 63ND–89ND.

Nabighian M.N., Grauch V.J.S., Hansen R.O., LaFehr T.R., Li Y., Peirce J.W. *et al*. 2005a. The historical development of the magnetic method in exploration. *Geophysics* **70**, 33ND–61ND.

Nabighian M.N. and Hansen R.O. 2001. Unification of Euler and Werner deconvolution in three dimensions via the generalized Hilbert transform. *Geophysics* **66**, 1805–1810.

Nelson J.B. 1986. An alternative derivation of the three-dimensional Hilbert transform relations from first principles. *Geophysics* **51**, 1014–1015.

Purucker M., Sabaka T., Le G., Slavin J.A., Strangeway R.J. and Busby C. 2007. Magnetic field gradients from the ST-5 constellation: Improving magnetic and thermal models of the lithosphere. *Geophysical Research Letters* **34**, L24306.

Ravat D. 1996. Analysis of the Euler method and its applicability in environmental magnetic investigations. *Journal of Environmental and Engineering Geophysics* **1**, 229–238.

Ravat D., Wang B., Wildermuth E. and Taylor P.T. 2002. Gradients in the interpretation of satellite-altitude magnetic data: An example from central Africa. *Journal of Geodynamics* **33**, 131–142.

Reid A.B., Allsop J.M., Granser H., Millett A.J. and Somerton I.W. 1990. Magnetic interpretation in three dimensions using Euler deconvolution. *Geophysics* **55**, 80–91.

Ricard Y. and Blakely R.J. 1988. A method to minimize edge effects in two-dimensional discrete Fourier transforms. *Geophysics* **53**, 1113–1117.

Sandwell D.T. and Smith W.H.F. 1997. Marine gravity anomaly from Geosat and ERS 1 satellite altimetry. *Journal of Geophysical Research* **102**(B5), 10039–10054.

Thomas M.D., Grieve R.A.F. and Sharpton V.L. 1988. Gravity domains and assembly of the North American continent by collisional tectonics. *Nature* **331**, 333–334.

Thompson D.T. 1982. EULDPH: A new technique for making computer-assisted depth estimates from magnetic data. *Geophysics* **47**, 31–37.

Wang Y.M. 2000. Predicting bathymetry from the Earth's gravity gradient anomalies. *Marine Geodesy* **23**, 251–258.

Wang B. 2006. 2D and 3D potential-field upward continuation using splines. *Geophysical Prospecting* **54**, 199–209.

Wang B., Krebes E.S. and Ravat D. 2008. High-precision potential field and gradient component transformations and derivative computations using cubic B-splines. *Geophysics* **73**, I35–I42.

Wessel P. and Smith W.H.F. 1995. New version of the Generic Mapping Tools released. *AGU Eos Transactions* **76**, 329.

APPENDIX A: UNIVARIATE CUBIC B-SPLINE INTERPOLATION

In the domain $D_1 = \{x | a \le x \le b\}$, make a partition

$$x_{-3} < x_{-2} < x_{-1} < x_0 = a < x_1 < \ldots < x_N = b < x_{N+1} < x_{N+2} < x_{N+3}.$$

The univariate cubic B-splines, whose interior knots are $\{x_i,\ i = 0, 1, \ldots, N\}$, can then be expressed as

$$S(x) = \sum_{i=-1}^{N+1} C_i N_i(x), \tag{A1}$$

where C_i are interpolation coefficients. The unified formula for interpolation, differentiation and integration is

$$S^u(x) = \sum_{i=-1}^{N+1} C_i N_i^u(x), \tag{A2}$$

where

$$N_i^u(x) = (x_{i+2} - x_{i-2}) B_i^u(x), \tag{A3}$$

and

$$B_i^u(x) = \frac{3!}{(3-u)!} \sum_{k=i-2}^{i+2} (-1)^u W_k (x_k - x)_+^{3-u}, \tag{A4}$$

$$W_k = \prod_{\substack{m=i-2 \\ m \neq k}}^{i+2} \frac{1}{x_k - x_m}, \tag{A5}$$

$$(x_k - x)_+^{3-u} = \begin{cases} (x_k - x)^{3-u}, & for \quad x \leq x_k \\ 0, & for \quad x > x_k \end{cases}. \tag{A6}$$

The u in equation (A2) has the following meaning: when u is a positive integer, calculate the uth-order derivative; when u is a negative integer, calculate the $|u|$th-order integral; when $u = 0$, do not calculate either derivative or integral, i.e. $N_i^0(x) = N_i(x)$.

$V(x)$ is a function defined in the domain D_1. $\{V(i),\ i = 0, 1, \ldots, N\}$ are known values of $V(x)$ at the interior knots. Use the univariate cubic B-splines (A1) to approximate $V(x)$ while satisfying the following conditions

$$S(x_i) = V(i), \quad i = 0, 1, \ldots, N, \tag{A7}$$

$$\frac{\partial S(x)}{\partial x} = \frac{\partial V(x)}{\partial x}, \quad at \quad x_0, \quad x_N. \tag{A8}$$

Substituting equation (A2) into equations (A7) and (A8), using a difference quotient to replace $\frac{\partial V(x)}{\partial x}$, and considering the localized nonzero characteristics of the cubic B-splines

$$N_i(x_k) = 0, \quad for \quad |i - k| > 1, \tag{A9}$$

yields

$$\mathbf{YC} = \mathbf{V}. \tag{A10}$$

where the dimensions are $\mathbf{Y}(N+3, N+3)$, $\mathbf{C}(N+3, 1)$ and $\mathbf{V}(N+3, 1)$.

From equation (A10) one obtains

$$\mathbf{C} = \mathbf{Y}^{-1}\mathbf{V}. \tag{A11}$$

i.e., the interpolation coefficients are determined.

APPENDIX B: BIVARIATE CUBIC B-SPLINE INTERPOLATION

In the domain $D_2 = \{(x, y) | a \leq x \leq b,\ c \leq y \leq d\}$, make a partition

$$\begin{aligned} x_{-3} < x_{-2} < x_{-1} < x_0 = a < x_1 < \ldots < x_{Nx} = b \\ < x_{Nx+1} < x_{Nx+2} < x_{Nx+3}. \\ y_{-3} < y_{-2} < y_{-1} < y_0 = c < y_1 < \ldots < y_{Ny} = d \\ < y_{Ny+1} < y_{Ny+2} < y_{Ny+3} \end{aligned}$$

The bivariate cubic B-splines, whose interior knots are $\{(x_i, y_j),\ i = 0, 1, \ldots, Nx,\ j = 0, 1, \ldots, Ny\}$, can be expressed as

$$S(x, y) = \sum_{i=-1}^{Nx+1} \sum_{j=-1}^{Ny+1} N_i(x) C_{i,j} N_j(y), \tag{B1}$$

where $C_{i,j}$ are interpolation coefficients. The unified formula for interpolation, differentiation and integration is

$$S^{u,v}(x, y) = \sum_{i=-1}^{Nx+1} \sum_{j=-1}^{Ny+1} N_i^u(x) C_{i,j} N_j^v(y), \tag{B2}$$

where $N_i^u(x)$ is shown in equation (A3), and $N_j^v(y)$ is similarly obtained for subscript j.

$V(x, y)$ is a function defined in the domain D_2. $\{V(i, j),\ i = 0, 1, \ldots, Nx,\ j = 0, 1, \ldots, Ny\}$ are known values of $V(x, y)$ at the interior knots. Use the bivariate cubic B-splines (B1) to approximate $V(x, y)$ while satisfying the following conditions

$$S(x_i, y_j) = V(i, j), \quad i = 0, 1, \ldots, Nx, \quad j = 0, 1, \ldots, Ny, \tag{B3}$$

$$\frac{\partial S(x, y)}{\partial x} = \frac{\partial V(x, y)}{\partial x}, \quad at \quad (x_0, y_j), \quad (x_{Nx}, y_j), \quad j = 0, 1, \ldots, Ny, \tag{B4}$$

$$\frac{\partial S(x, y)}{\partial y} = \frac{\partial V(x, y)}{\partial y}, \quad at \quad (x_i, y_0), \quad (x_i, y_{Ny}), \quad i = 0, 1, \ldots, Nx, \tag{B5}$$

$$\frac{\partial^2 S(x, y)}{\partial x \partial y} = \frac{\partial^2 V(x, y)}{\partial x \partial y}, \quad at \quad (x_0, y_0), \quad (x_0, y_{Ny}), \quad (x_{Nx}, y_0), \quad (x_{Nx}, y_{Ny}). \tag{B6}$$

Substituting equation (B2) into equation (B3–B6), using difference quotients to replace $\frac{\partial V(x,y)}{\partial x}$, $\frac{\partial V(x,y)}{\partial y}$ and $\frac{\partial^2 V(x,y)}{\partial x \partial y}$, and considering the localized nonzero characteristics of the cubic B-splines (A9), yields

$$\mathbf{XCY} = \mathbf{V}. \tag{B7}$$

where the dimensions are $\mathbf{X}(Nx+3, Nx+3)$, $\mathbf{C}(Nx+3, Ny+3)$, $\mathbf{Y}(Ny+3, Ny+3)$ and $\mathbf{V}(Nx+3, Ny+3)$.

From equation (B7) one obtains

$$\mathbf{C} = \mathbf{X}^{-1}\mathbf{V}\mathbf{Y}^{-1}. \tag{B8}$$

i.e., the interpolation coefficients are determined. Because of the localized feature of the cubic B-splines, a large matrix is decomposed into two much smaller matrixes. The computations are fast.